JGR Space Physics

Key Points:

- Loss processes influencing >0.63 MeV electrons are enhanced outside the plasmapause during storm main phase
- Enhanced loss processes are sustained throughout the recovery phase on the dawnside but diminish early in storm recovery phases across dusk
- Analyzing loss enhancements as a function of L, MLT, and AE may indicate wave influences including whistler-mode chorus and plasmaspheric hiss

Correspondence to:
S. D. Walton,
samuel.walton.18@ucl.ac.uk

Statistical Comparison of Electron Loss and Enhancement in the Outer Radiation Belt During Storms

S. D. Walton[1] , **C. Forsyth[1]** , **I. J. Rae[2]** , **N. P. Meredith[3]** , **J. K. Sandhu[2]** , **M.-T. Walach[4]** , and **K. R. Murphy[2]**

[1]Mullard Space Science Laboratory, University College London, Dorking, UK, [2]Department of Maths, Physics, and Electrical Engineering, Northumbria University, Newcastle Upon Tyne, UK, [3]British Antarctic Survey, Cambridge, UK, [4]Physics Department, Lancaster University, Lancaster, UK

Abstract The near-relativistic electron population in the outer Van Allen radiation belt is highly dynamic and strongly coupled to geomagnetic activity such as storms and substorms, which are driven by the interaction of the magnetosphere with the solar wind. The energy, content, and spatial extent of electrons in the outer radiation belt can vary on timescales of hours to days, dictated by the continuously evolving influence of acceleration and loss processes. While net changes in the electron population are directly observable, the relative influence of different processes is far from fully understood. Using a continuous 12 year data set from the Proton Electron Telescope on board the Solar Anomalous Magnetospheric Particle Explorer, we statistically compare the relative variations of trapped electrons to those in the bounce loss cone (BLC). Our results show that there is a proportional increase in flux entering the BLC outside the plasmapause during storm main phase and early recovery phase. Loss enhancement is sustained on the dawnside throughout the recovery phase while loss on the duskside is enhanced around minimum Sym-H and quickly diminishes. Spatial variations are also examined in relation to geomagnetic activity, making comparisons to possible causal wave modes such as whistler-mode chorus and plasmaspheric hiss.

1. Introduction

Earth's outer Van Allen radiation belt is a highly dynamic environment, dictated by acceleration, loss, and transport of extremely energetic electrons (reviewed in Friedel et al., 2002). Electron variability over multiple orders of magnitude can take place over timescales ranging from a few hours to several days and weeks, associated with periods of geomagnetic disturbance such as storms (e.g., Borovsky & Denton, 2009; Reeves et al., 2003) and substorms (e.g., Forsyth et al., 2016). Enhancements in the high energy ($\gtrsim$300 keV)) electron population can result from localized processes on timescales of a few hours, such as interaction with very-low frequency chorus waves generated as a result of lower energy ($\approx$100 eV–100 keV) particle injections into the outer radiation belt (e.g., Horne & Thorne, 1998; Thorne, 2010). Locally accelerated electrons subsequently undergo azimuthal drift and both inward and outward radial diffusion, reducing the local peak in energization. Inward radial diffusion therefore contributes to the enhancement of larger areas of the outer radiation belt, though typically over larger timescales (e.g., Lejosne & Kollmann, 2020; Loto'aniu et al., 2006; Mann et al., 2016; Olifer et al., 2019). Many of the outwardly diffusing particles become vulnerable to loss to the outer magnetosphere, as the dayside magnetopause can become compressed during times of increased geomagnetic activity and quickly reducing the electron population at a large range of energies. Electrons can also be lost by pitch angle scattering by a variety of wave modes including plasmaspheric hiss (e.g., Meredith et al., 2007), electromagnetic ion cyclotron (EMIC) waves (e.g., Ross et al., 2020), and chorus waves (e.g., Reidy et al., 2021; Thorne et al., 2013), resulting in their precipitation into the atmosphere. Ultralow frequency (ULF) waves can contribute to this precipitation of electrons over a larger area via direct modulation of the bounce loss cone (BLC; Brito et al., 2015; Rae et al., 2018). Further loss processes are comprehensively reviewed in Millan and Thorne (2007).

While whistler-mode chorus waves play a dual role in outer radiation belt electron dynamics (Bortnik & Thorne, 2007), contributing to both acceleration and loss, plasmaspheric hiss and EMIC waves are primarily loss mechanisms. Chorus waves are thought to play an important part in the generation of plasmaspheric hiss (Bortnik et al., 2008), a structureless, broadband whistler-mode wave confined inside the plasmasphere, predominantly on the dayside (Meredith, Horne, Clilverd, et al., 2006; Meredith et al., 2018; Thorne et al., 1973). Plasmaspheric hiss waves contribute to electron loss during geomagnetic storms (e.g., Lam et al., 2007; Summers et al., 2007)

and can explain the quiet time decay of outer radiation belt electrons (e.g., Meredith, Horne, Glauert, et al., 2006). Hiss waves are also thought to be responsible for the formation of the slot region (Breneman et al., 2015; Meredith et al., 2007; Smith et al., 1974; Tsurutani et al., 1975).

EMIC waves, which occur at lower frequencies (0.1–5.0 Hz) than that of whistler-mode chorus and hiss waves can also be effective at scattering pitch angles of energetic electrons. EMIC waves are generated from proton distribution anisotropies ($T_\perp > T_\parallel$) related to overlapping cold and hot ion populations (such as at the duskside plasmapause; Kozyra et al., 1984; Lyons & Thorne, 1972; Thorne, 2010). EMIC wave activity is enhanced during storm time (e.g., Halford et al., 2010; Wang et al., 2019) and periods of heightened geomagnetic activity, typically being most intense in the post-noon through dusk region at $L > 4.0$, though they have been observed near dawn (Halford et al., 2016; Meredith et al., 2014; Usanova et al., 2012; Zhang et al., 2016). EMIC waves have been observed as possible causes of relativistic (MeV) electron pitch angle scattering (e.g., Bortnik et al., 2006; Sigsbee et al., 2020) and subsequent precipitation into the atmosphere (e.g., Qin et al., 2018; Rodger et al., 2015). More recent studies provide evidence of sub-MeV EMIC precipitation (Blum et al., 2015; Clilverd et al., 2015; Hendry et al., 2017, 2021, 2019), suggesting that EMIC scattering is not exclusive to MeV energies, but act over a larger range. However, there are studies providing evidence that EMIC activity can be enhanced without subsequent precipitation (e.g., Engebretson et al., 2015; Usanova et al., 2014). There have also been recent suggestions that the combined effect of simultaneously occurring EMIC and whistler-mode chorus waves could effectively scatter electrons into the loss cone when occurring on the same particle drift path (Lee & Kim, 2020). The combined behavior of EMIC waves, whistler-mode chorus, hiss, and other geomagnetic waves in relation to geomagnetic activity is far from fully understood, nor is their precise link to acceleration, scattering, and subsequent precipitation of relativistic and near-relativistic electrons.

Studies have attempted to shed light on the net variation of electrons during storm time in relation to the above mentioned waves. Reeves et al. (2003) analyzed the response of the radiation belts to 276 moderate and intense geomagnetic storms, finding a mix of responses. Just 53% of storms resulted in an overall increase in radiation belt flux of MeV electrons. The response of the other events was a mix between a reduction in fluxes and very little change at all. Other studies have though, categorized storms as either geoeffective or non-geoeffective based on the response of the radiation belts. Meredith et al. (2003, 2002) categorize storms in terms of IMF B_Z and substorm activity respectively, linking positive IMF B_z to a reduced recovery of electron fluxes during the recovery phase, particularly for electrons >1 MeV, which could be attributed to a lack of substorm activity. Miyoshi and Kataoka (2008) investigate the geoeffectiveness of stream interaction regions in relation to the radiation belts, as opposed to other driving mechanisms such as coronal mass ejections and found that while solar wind speed plays a significant role in flux enhancement, it is not sufficient by itself. Murphy et al. (2018) statistically examine the repeatability of storms in adiabatic invariant coordinates (μ, K, and L^*), categorizing the dynamics into an initial phase dominated by loss, followed by a second phase dominated by acceleration after the time of minimum Sym-H.

The relative makeup of the different acceleration and loss processes in and following a given event or set of events, has proven to be very complex and varied in nature. Multiple simultaneous measurements are required to see the entire picture of an event, which often is only available by chance and therefore such observations are only sporadically available, though some studies have taken advantage of these occurrences (e.g., Crew et al., 2016; Halford et al., 2015; Hendry et al., 2019). Halford et al. (2015) for example, were able to observe particle and magnetic field variations in space following the January 2014 storm using Van Allen Probes A and B, as well as GOES 13 and 15. All were within a few MLT and L of each other. The resulting electron precipitation was also measured from the upper atmosphere using the Balloon Array for Radiation belt Relativistic Electron Losses mission. Many studies have taken advantage of low-altitude spacecraft and their ability to measure precipitating flux, and compared these with wave measurements or statistics (Carson et al., 2013; Hardman et al., 2015; Lam et al., 2010), or with ground-based instruments capable of observing the atmospheric effects of electron precipitation (Dietrich et al., 2010; Rodger, Carson, et al., 2010; Rodger, Clilverd, Green, & Lam, 2010). Low-altitude spacecraft from the NOAA Polar Operational Environmental Satellite (POES) mission has some limited capability to observe both precipitating fluxes and trapped fluxes simultaneously, though a meaningful comparison is only possible through statistical means (e.g., Meredith et al., 2011), and there are limited analyses for particles >1 MeV. The POES Medium Energy Proton and Electron Detector instrument also only measures a small fraction of the atmospheric loss cone due to the small angular field of view compared to the relatively large local

loss cone. Reidy et al. (2021) showed the potential to reconstruct the loss cone using the measured flux data and equations from Kennel and Petschek (1966) and comparing to the modeled fluxes calculated using BAS-RBM diffusion coefficients (Glauert et al., 2014).

In this study, we address the lack of available comparisons between trapped and precipitating electrons, particularly at energies close to and above 1 MeV by statistically comparing trapped and BLC fluxes. We use 12 yr data set from the Proton/Electron Telescope (PET; Cook et al., 1993) aboard the Solar Anomalous Magnetospheric Particle Explorer (SAMPEX) mission (Baker et al., 1993) to statistically analyze variations in energetic electron flux during geomagnetic storms. We present a superposed epoch analysis (SEA) to statistically compare measurements of precipitating and trapped electrons >0.63 MeV by means of the ratio of precipitating flux to trapped flux in order to examine the relative variation between the two. In Section 4, we parameterize all 12 yr of flux measurements by the AE index to provide an insight into the L-MLT variation of trapped and BLC fluxes during differing levels of geomagnetic activity. Section 5 provides an in-depth discussion of the results, including detailed comparison with previously studied wave statistics, potentially the cause of enhanced loss.

2. Instrumentation and Data

The data sets used in this study are derived from the PET, one of the four scientific instruments on NASA's SAMPEX mission. SAMPEX was a low-altitude small explorer spacecraft operating at altitudes in the region of 400–700 km, beginning closer to 700 km and slowly descending throughout the mission. SAMPEX's orbital period was approximately 90 min, inclined at 82°. Twelve-years of 6 s data from 1992 to 2004 are used from PET's low energy electron channel, originally described as measuring 1.5–6.0 MeV electron flux (Cook et al., 1993). However, Selesnick (2015) showed that PET is susceptible to contamination from high energy protons and electrons with energies as low as 0.63 MeV when passing through the highly intense outer radiation belt. Proton contamination is not a concern for our analysis because we do not consider the inner belt, but lower energy electron contamination must be considered. We, therefore, consider it likely that PET was measuring particles >0.63 MeV and we refer to the data as such.

The SAMPEX spacecraft orbit provided measurements of relativistic electron flux inside the BLC and drift loss cone (DLC), the range of pitch angles in which a particle is likely to be lost to the atmosphere inside a few bounce periods or inside one drift period, respectively. PET's wide-angle (58°) field of view has the advantage of seeing a much larger portion of the loss cone than that seen from the POES satellites. PET also regularly viewed pitch angles large enough to capture a significant number of trapped electrons. SAMPEX's longevity provides us with enough data (12 yr) to be able to statistically compare the trapped electron population to that which is lost and ultimately precipitated into the atmosphere.

In order to compare BLC flux to trapped flux, we must determine with reasonable confidence which of the populations PET was observing at any given time. Using IGRF magnetic field values local to SAMPEX, we approximate the spacecraft's location within the field relative to the stable trapping region for electrons, as well as calculating the size of the BLC and DLC. We then use spacecraft attitude data to determine the percentage of the 58° field of view that was covering pitch angles either in the BLC, or pitch angles outside the DLC and therefore trapped. Note that we do not consider particles with pitch angles greater than the BLC that are also smaller than the DLC.

Figure 1 shows the processing explained above. Figure 1a shows the percentage of PET's 58° field of view that was seeing flux in the BLC, while Figure 1b shows this for trapped flux, plotted against geographical location. The data shows the mean percentage in each 1° × 1° geodetic coordinate bin for the year of 1998 to give a demonstration of the populations that were being observed by PET. Coverage of the BLC, shown in Figure 1a, is relatively extensive, as would be expected from a low-altitude spacecraft. Generally, PET always captured part of the BLC, with upwards of 70%–80% of the field of view inside the BLC in much of the Northern and Southern Hemispheres. In the northern Atlantic and Europe region of the map, PET's field of view is 100% inside the BLC, meaning that these particles are the only ones entering the detector and are isolated from other populations. This region is where the spacecraft is magnetically conjugate to the South Atlantic Anomaly (SAA) region, so the particles which PET observes here should precipitate within a few bounce motions (typically a few milliseconds). Due to the 90 min orbit and the rotation of the Earth, SAMPEX passed through this region multiple times per day,
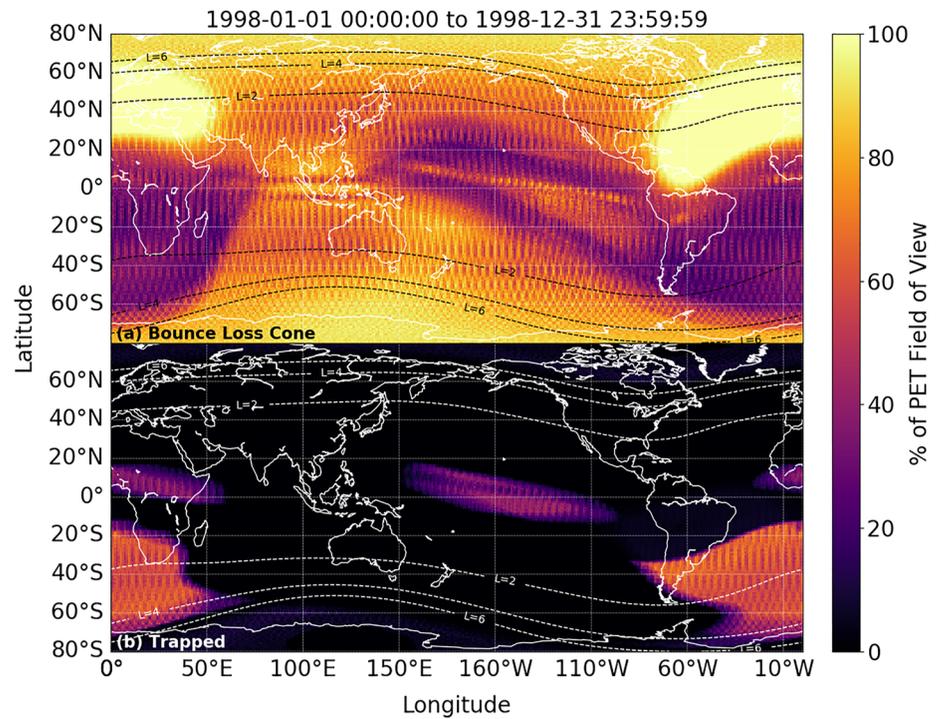
Figure 1. World maps in geodetic coordinates, showing the percentage of the 58° field of view of Proton Electron Telescope (PET) that was seeing (a) flux in the bounce loss cone and (b) trapped flux. Latitude-longitude bins are $1° \times 1°$ in size, each containing the mean percentage for the year 1998. The dashed lines show $L = 2$, $L = 4$, and $L = 6$ as labeled.

providing enough data to isolate and form the BLC only data set. It is noted that while the pitch angle distribution of MeV particles inside the BLC is unlikely to be isotropic, we assume that due to the large field of view provided by PET, enough of the distribution is covered to be representative of the average BLC.

Figure 1b shows the percentage of PET's field of view which is observing trapped flux. It is immediately clear that trapped flux measurements are almost exclusively taking place in the SAA region and much less common than measurements of flux in the BLC or DLC. It is also apparent that there are no regions in which PET observed only trapped particles. In the SAA region, the trapped flux commonly makes up around or above 60% of the field of view and may exceed 80% in some cases. To produce the trapped flux data, we assume that trapped flux is at least an order of magnitude more intense than flux in the BLC or DLC and that therefore the BLC or DLC fluxes are negligible when being observed at the same time as trapped. Multiplying the observed flux by the inverse of the fraction of the field of view observing trapped flux provides the final trapped flux value. For example, if the coverage was 50% trapped, we would multiply that measurement by 2 in order to "fill" the detector to 100%, assuming the other 50% containing non-trapped particles were negligible. Eighty percent coverage would be multiplied by 1.25 and so on. Should the trapped flux coverage reach levels as low as 10% for example, the assumption that it is at least an order of magnitude more intense is brought into question, as the share of trapped to non-trapped flux would be 10%–90%. We, therefore, set a limit of 30% trapped flux in the detector (or a correction factor of $3.3\dot{3}$) as a reasonable minimum coverage for the mentioned assumption to be true, though as Figure 1b shows, the great majority of observations in this region contain ≥60% trapped flux. Even without the assumption of negligible non-trapped flux, this would only result in a small overestimate of the trapped flux, which is inconsequential in our interpretation of the results, as we draw conclusions from the statistical trends rather than absolute values. The features shown in Figure 1 are in agreement with previous studies which have attempted to determine the different populations observed by low altitude spacecraft (e.g., Dietrich et al., 2010; Rodger, Carson, et al., 2010; Rodger, Clilverd, et al., 2010; Rodger et al., 2013; Selesnick, 2015), including the HILT instrument (Klecker et al., 1993) aboard SAMPEX.
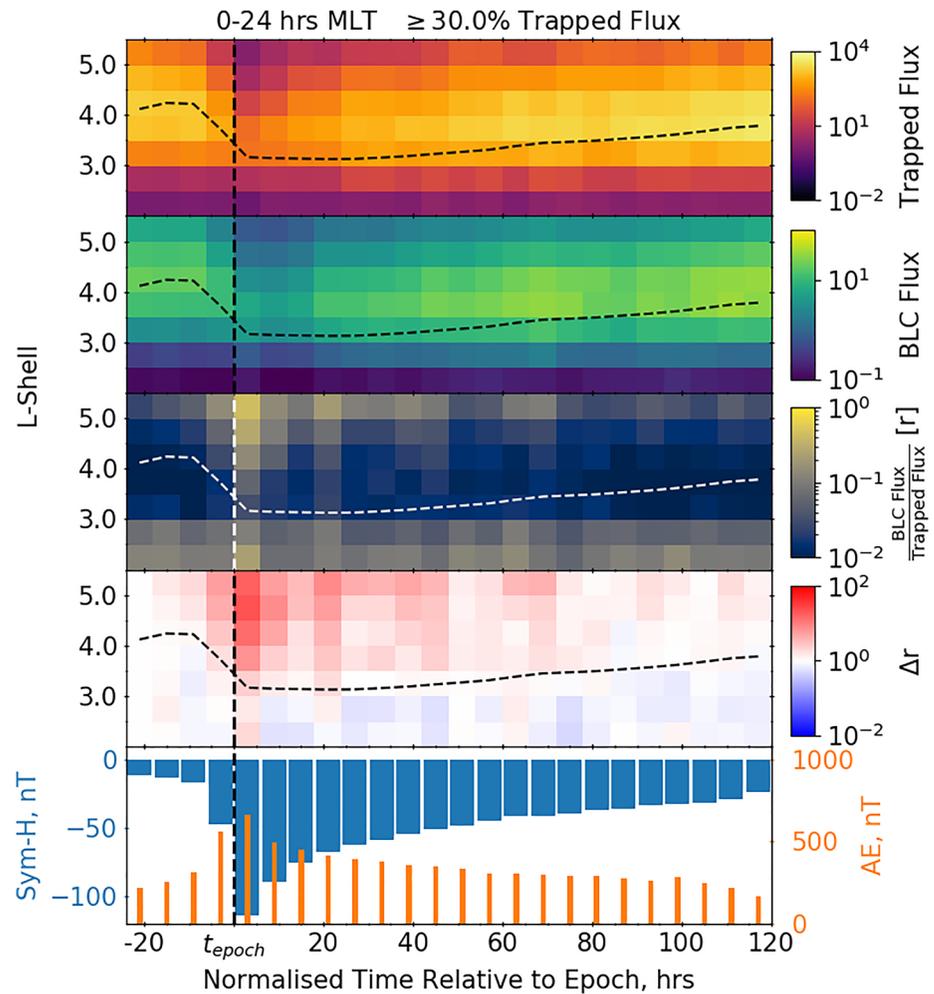
3. Superposed Epoch Analysis

In this section, we present a statistical analysis of >0.63 MeV electron dynamics throughout 168 storms within our 1992–2004 period of SAMPEX/PET observations. Using the algorithm described in Walach and Grocott (2019) for the Sym-H index, we define three epoch times per storm; the start of the storm (start of the initial phase), the epoch time t_{epoch} (beginning of the recovery phase), and the end of the storm. The end of the storm for this analysis is considered to be the end of the recovery phase, plus 50% additional time per storm in order to capture the continuing behavior of the electron fluxes beyond the algorithm's definition. We group together initial and main phases between the start of the storm and t_{epoch} in order to increase data coverage. It is also important to consider that throughout the 168 storms, there is significant variation in the length of each phase. We, therefore, normalize the time between the start of the initial phase and the start of the recovery phase and the time between the start and end of the recovery phase separately (e.g., Halford et al., 2010; Hutchinson et al., 2011; Murphy et al., 2018; Yokoyama, 1997) such that data from all respective phases are combined. We effectively "stretch" or "compress" each storm so that all are the same length with an initial and main phase lasting 24 "hr" along the normalized timeline and a recovery phase lasting 120 "hr". We align each of the three epochs such that the storm begins at −24 hr and ends at +120 hr, 0 hr (t_{epoch}) being the time of the start of the recovery phase. We then bin fluxes by L-shell and time and calculate the mean of the $\log_{10}$(flux). Note that when referring to time (in hours) in this analysis from now on, we are referring to the normalized time as described and not "real" time.

Figure 2 shows the results of the SEA of the 168 geomagnetic storms, binned in 6 hr intervals relative to t_{epoch} along the normalized time axis and 0.5 L-shell for $L = 2.0–5.5$, for all 0–24 hr in MLT. This L-shell range was chosen to both remove the effects of proton contamination below $L = 2.0$ and remove regions of low trapped flux coverage outside $L = 5.5$, which would distort the result. The vertical dashed lines show the t_{epoch} time and the variable dashed lines show the mean plasmapause location for the labeled MLT range, calculated using the O'Brien and Moldwin (2003) model. The top and second panels show >0.63 MeV trapped flux and BLC flux respectively. Both show broadly what is expected during a geomagnetic storm; a period of loss during the main phase (6–12 hr before t_{epoch}) shown by the reduction in BLC and trapped fluxes at most L-shell, followed by a period of enhancement during the recovery phase shown by the recovery of flux to approximately equal to (or higher than) pre-storm levels during this time. This is also in agreement with Murphy et al. (2018) who show a net loss phase in total radiation belt electron content, followed by an acceleration phase resulting in a net increase.

The third panel in Figure 2 shows the ratio of BLC flux to trapped flux. If we consider that the active loss processes at a given time act to scatter a proportion of the trapped flux into the BLC, then this proportion should remain constant as long as there is no change in the loss processes. That is the variation in the BLC flux should directly track the variation of the trapped flux. However, if the loss processes vary, the proportion of the trapped flux which enters the BLC should change, and thus so should the ratio of BLC to trapped flux, which we refer to as r. An increase in r would therefore indicate an enhancement in the loss processes acting upon the population. Likewise, a decrease in r would indicate a reduction in those loss processes. The fourth panel down shows the change in r relative to the first time bin of the storm (−24 to −18 hr), which we refer to as Δr. Red indicates that r is higher than the initial level (enhanced loss processes), and blue indicates that r is lower than at the initial level (reduced loss processes). The bottom panel shows the SEA of the Sym-H index (blue) and the AE index (orange), both 6 hr binned in normalized time.

The variation in r shown by the third panel down in Figure 2 indicates how the effect of loss processes tend to vary throughout a storm. r remains below 0.1 for large parts of the storm (the BLC flux is small in comparison the trapped flux), but around t_{epoch} increases to a peak of around 0.25 at the higher L-shells, indicating an enhancement in loss processes. r is consistently closer to 1 inside $L = 3.0$ due to the comparatively low fluxes in both the BLC and the trapped population. As both populations tend toward the noise floor of the instrument, the ratio of BLC to trapped flux tends toward 1; however, this still shows the well-known slow but relatively constant loss effect of plasmaspheric hiss (e.g., Meredith, Horne, Glauert, et al., 2006). In the fourth panel down, the temporal variation across the storm is shown more clearly. Outside the plasmapause, Δr increases (loss processes are enhanced) by around two orders of magnitude during the initial and main phase (−24 hr to t_{epoch}) through to 0–6 hr post-t_{epoch}, where it reaches a peak. Δr then gradually reduces throughout the recovery phase back to approximately initial levels. The plasmapause (and therefore the mentioned variations in Δr) moves inwards from outside $L = 4.0$ to around $L = 3.0$ during the latter period of the initial and main phase, and gradually increases in extent again throughout the recovery phase to around $L = 4.0$. Inside the plasmapause, the changes are much
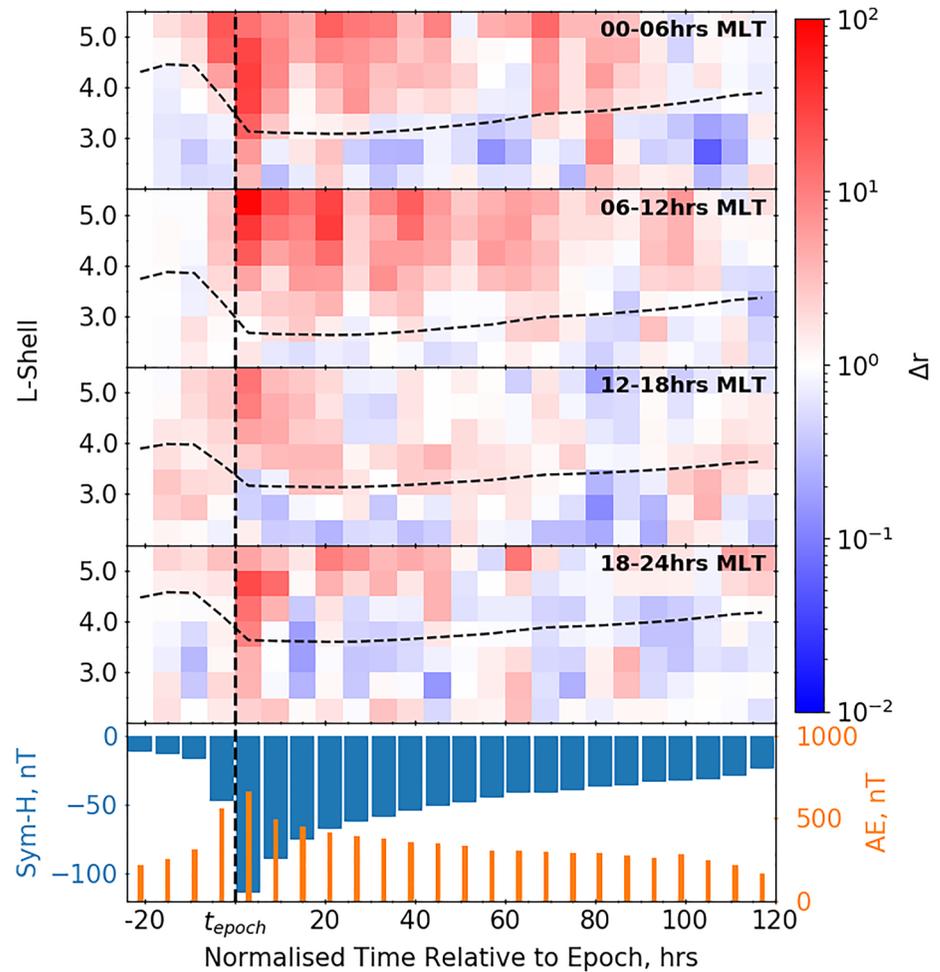
Figure 2. Superposed epoch analysis (SEA) results of 168 storms along a normalized time axis binned by 6 hr and 0.5 L-shell, for 0–24 hr in MLT. The vertical dashed line shows the epoch time, t_{epoch}, and the varying dashed lines represent the mean model plasmapause location, calculated from the O'Brien and Moldwin (2003) model. The top four panels show >0.63 MeV trapped electron flux, >0.63 MeV bounce loss cone (BLC) electron flux (measured in $cm^{-2} \, s^{-1} \, sr^{-1}$), the ratio of BLC to trapped flux, and the variation in the ratio from the initial level of r (Δr). The bottom panel shows the SEA for both Sym-H (blue) and AE (orange).

smaller; however, we do observe an increase in Δr immediately after t_{epoch} of less than an order of magnitude, followed by a similar sized decrease for the remainder of the storm. The Sym-H and AE indices remain consistent with what is to be expected during a storm, with activity maximizing in magnitude around t_{epoch} and reducing throughout the recovery phase.

Figure 3 shows the same analysis as in Figure 2 but separated into MLT quadrants in Δr to examine storms in more spatial detail. From the first to fourth panel, 0–6, 6–12, 12–18, and 18–24 hr in MLT are shown respectively. Note that the plasmapause is now averaged over the corresponding MLT quadrant, rather than all MLT. The bottom panel shows the superposed Sym-H and AE indices identically to before. Figure 3 highlights notable differences between how Δr varies in the different MLT sectors. In the 0–6 and 6–12 MLT sectors (dawnside), Δr varies in a similar way to that observed in Figure 2, where Δr increases by around two orders of magnitude outside the plasmapause, peaking in the 0–6 hr bin and reduces for the remainder of the recovery phase. Inside the dawnside plasmapause, we observe a more pronounced reduction in Δr than in Figure 2.

Variations in Δr are different on the duskside to that of the dawnside. Both duskside MLT quadrants (12–18 and 18–24 MLT) still show an increase in Δr, peaking around t_{epoch}, but reduces to smaller, less consistent variation

Figure 3. Superposed epoch analysis (SEA) Δr quantity calculated as in Figure 2, separated into MLT quadrants. The vertical dashed line shows the epoch time, t_{epoch}, and the varying dashed lines represent the mean plasmapause location, calculated from the (O'Brien & Moldwin, 2003) model. The first, second, third, and fourth panels show 0–6, 6–12, 12–18, and 18–24 hr in MLT respectively. The bottom panel shows the SEA for both Sym-H (blue) and AE (orange).

early on in the recovery phase. The peaks in Δr are also smaller than on the dawnside, reaching closer to a single order of magnitude increase rather than two. Duskside variations do not appear to have any relationship to the plasmapause, which could indicate a process that acts irrespective of the location of the plasmapause, but alternatively, could be a feature of the plasmapause model. The O'Brien and Moldwin (2003) model plasmapause does not take into account the maximum effect of duskside plasmasphere distortion and cold plasma such as that resulting from plasmaspheric drainage plumes, which could influence the dynamics of duskside electrons (e.g., Goldstein et al., 2004; Usanova et al., 2013).

We have analyzed the changing dynamics of >0.63 MeV electrons in the outer radiation belt throughout geomagnetic storms. Statistically comparing flux in the BLC to trapped flux by calculating the ratio has provided an insight into the relative variation of the two populations and therefore the changing proportion of flux which ultimately becomes lost to the atmosphere. We have shown that on the dawnside magnetosphere between $L = 2.0$–5.5, Δr is consistently enhanced throughout the storm outside the plasmapause, peaking around t_{epoch} (minimum Sym-H) and reducing throughout the recovery phase to similar levels as the beginning of the storm. Inside the plasmapause, there is a slight reduction in Δr. The duskside enhancements are less clear, but still show increased Δr around t_{epoch}.
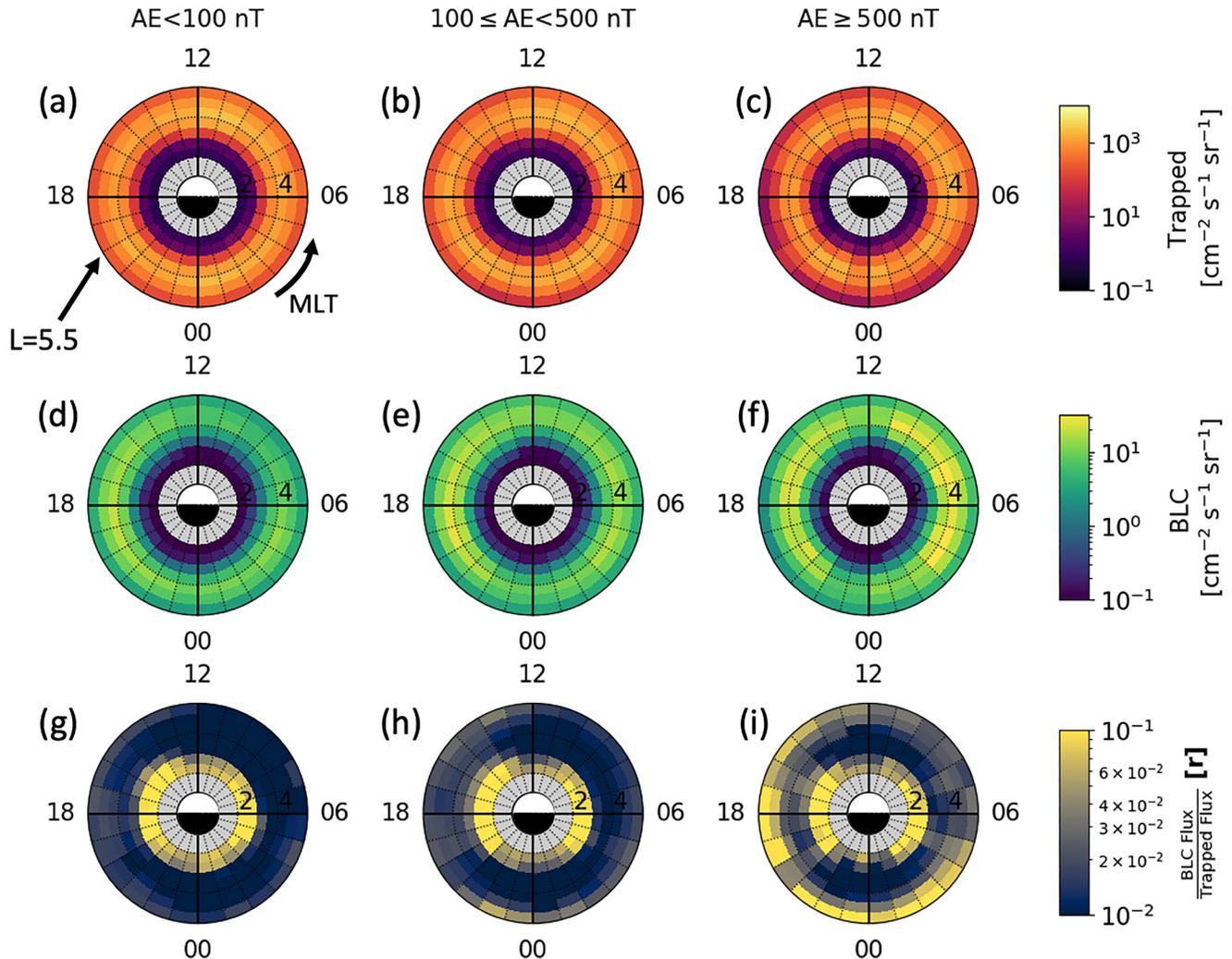
Figure 4. >0.63 MeV L-shell vs. MLT plots from $L = 2.0$–5.5 of; (a–c) trapped flux, (d–f) bounce loss cone (BLC) flux and (g–i) the ratio of BLC flux to trapped flux, r. Data is parameterized by the AE index as; (a, d, g) AE < 100 nT, (b, e, h) $100 \leq$ AE < 500 nT and (c, f, i) AE ≥500 nT. The areas inside $L = 2.0$ are shaded gray due to possible proton contamination.

4. Relative Variations as a Function of L, MLT, and AE

So far, we have analyzed relative variations of trapped and BLC >0.63 MeV electron flux during storm time, and separated this into MLT quadrants. In this section, we consider trapped and BLC fluxes as a function of L, MLT, and geomagnetic activity, plotting all flux data from 1992 to 2004. We use the AE index to parameterize measurements by geomagnetic activity, regardless of storm activity.

Figure 4 shows >0.63 MeV electron fluxes as a function of L-shell and MLT. All data from 1992 to 2004 are binned in 0.5 L intervals in the L range of 2.0–5.5 and 24 hr of MLT in 1 hr intervals in MLT and the means of the $\log_{10}$ values are calculated. The areas inside $L = 2.0$ are shaded gray due to the possibility of proton contamination from the inner radiation belt. Plots (a–c) show trapped flux, plots (d–f) show flux in the BLC and plots (g–i) show the ratio of the mean BLC flux to the mean trapped flux, r. Plots (a, d, and g) show data for AE < 100 nT (low activity), plots (b, e, and h) show data for $100 \leq$ AE < 500 nT (moderate activity) and plots (c, f, and i) show data for AE ≥ 500 nT (high activity).

The plots of trapped flux, regardless of AE, clearly show the high-intensity region of the outer radiation belt, peaking between fluxes of 10^3 and 10^4 cm^{-2} s^{-1} sr^{-1} at $L = 4.0$. With increasing AE, we observe little change in the core of the outer belt ($L = 3.0$–5.0), but there is a reduction in trapped flux in the outermost region ($L > 5.0$),

particularly on the nightside (bottom). In the BLC, variation with AE is more obvious (noting that the color scale is narrower). Low activity BLC fluxes mostly do not reach intensities above $10^1 \, \text{cm}^{-2} \, \text{s}^{-1} \, \text{sr}^{-1}$ other than around 14–22 MLT through dusk and $L = 3.0$–5.0 which becomes more intense with increasing AE. Also with increasing AE, a second region emerges between 3 and 11 MLT through dawn and at $L = 3.0$–5.0, most prominent during periods of high activity. In the plots of r, we are able to analyze how the above mentioned variations in trapped and BLC flux vary in relation to each other. At all levels of activity, r is comparatively high ($\approx 10^{-1}$), resulting from the low fluxes observed in both trapped and BLC populations in the slot region, but still shows the increased loss as may be expected from the presence of plasmaspheric hiss. During low activity, this is the only prominent region, but with increasing AE, multiple features emerge; at $L > 5.0$ on the nightside, r increases by around one order of magnitude from low to high activity. This is resulting from the reduction in trapped flux in the same region as mentioned, where there is no change in BLC flux, indicating the enhancement of one or more loss processes. The second prominent increase in r is around 14–21 MLT through dusk and $L > 3.0$, resulting from the increasing BLC flux where there is no change in trapped flux. The loss processes appear to have enhanced the most, by around a half to one full order of magnitude in r, in the outer region ($L > 5.0$). Finally, we also observe increasing r outside of around $L = 2.5$–3.0 in all other regions, seen most clearly in the pre-noon sector (6–12 MLT) due to the lack of other prominent features. We observe a very low r (10^{-2}) during periods of low AE activity, but this increases by more than half an order of magnitude during periods of high activity, corresponding to the dawnside increase in BLC flux, where it is clear there is no similar increase in the trapped population.

In this section, we have statistically compared BLC and trapped flux as a function of L-shell and MLT. Variations in r clearly show that there are a multitude of loss processes that come into effect with increasing AE, affecting different regions of the outer radiation belt. The results of this analysis could be linked to similar processes driving the variations in the storm SEA, particularly at the higher levels of activity. The two analyses differ during moderate activity, as the sustained dawnside loss in the SEA is not captured in the L-MLT maps. This could suggest an effect that is restricted to only storm times and not produced by substorm activity, or that parameterizing by AE hides some of the activity.

5. Discussion

Understanding the complex dynamics of the outer radiation belt is essential in order to build models capable of making accurate predictions of behavior. Particle dynamics and the processes which influence those particles are integral to this and directly comparing different acceleration and loss processes can be difficult with current data availability. We have attempted to identify enhancements in atmospheric loss processes by examining changes in the ratio of flux in the BLC to trapped flux, r, and the change in r compared to the beginning of the storm, Δr.

In the first part of our analysis, we statistically analyze the dynamics of storm time >0.63 MeV electrons via a SEA. 168 storms were used, generated via the algorithm described in Walach and Grocott (2019) and superposed onto a normalized timeline using three epochs (start, minimum Sym-H, and end), where the mean of both BLC and trapped fluxes binned by L-shell and normalized "time" were calculated. This approach addresses the problem whereby differing lengths of storms averaged about a single, fixed epoch can mask physical features in the data. For 0–24 hr MLT (Figure 2), Δr increases by ≈ 2 orders of magnitude during the initial and main phase (pre-t_{epoch}) through to the +0–6 hr period, reaching a peak here. This is followed by a reduction of Δr back to initial levels across the recovery phase. It is clear in the top panel showing the reduction in trapped flux at most L-shell that statistically, loss processes are dominant during this period. Following $t_{\text{epoch}} + 6$ hr, trapped flux increases again as the enhancement of Δr reduces, signaling a reduction in the loss processes and a phase dominated by acceleration mechanisms. The analysis in Murphy et al. (2018), using a similar SEA technique, arrives at similar conclusions. Though the mentioned study resolves for non-adiabatic changes (which we cannot do with SAMPEX/PET), the implications on electron flux at > 0.63 MeV energies and at a range of L-shells are shown here. It is also important to emphasize that our analysis is an average of many storms, which would hide effects specific to a particular type of storm. As found by Reeves et al. (2003), storms may result in a net loss of electrons, a net increase, or close to no change at all.

Figure 2 shows a clear distinction between the relative behaviors of electrons outside and inside the mean plasmapause location. Walton et al. (2021) has shown that trapped flux varies coherently but differently inside and outside the plasmapause. However, the study also shows that trapped flux coherence may be unrelated to the

plasmapause during storm times, but here the distinction between flux inside and outside the plasmapause remains clear when comparing that of the BLC and trapped populations. The consistently high relative loss inside the plasmapause is indicative of plasmaspheric hiss waves. Hiss waves are thought to be responsible for the formation of the slot region due to their consistent, slow loss effects on energetic electrons (e.g., Meredith et al., 2007; Smith et al., 1974; Tsurutani et al., 1975).

Figure 3 shows Δr throughout a storm as before, but separated into four MLT sectors. The trend in the dawn sectors (0–6 and 0–12 MLT) is similar to that of the 0–24 hr analysis, but more visibly pronounced. Relative loss outside the plasmapause rapidly increases during the pre-t_{epoch} phase and peaks in the 0–6 hr following t_{epoch}. Relative loss then gradually decreases during the recovery phase, showing the acceleration-dominated phase of the storm. Δr in duskside sectors (12–18 and 18–24) still show increased Δr around pre-t_{epoch} +6 hr, but declines again very early in the recovery phase and becomes small and inconsistent. This suggests, unsurprisingly, that many of the processes influencing outer belt electrons around dawn are less active on the duskside. The plasmapause seems to be less influential on >0.63 MeV electrons around dusk, but could be a consequence of the O'Brien and Moldwin (2003) model, which does not take into account the maximum effect of duskside plasmasphere distortion and plasmaspheric drainage plumes. Whistler-mode chorus waves are thought to be prominent drivers of dawnside electron precipitation, in part due to relativistic (or near-relativistic) electron microbursts (e.g., Dietrich et al., 2010; Douma et al., 2017; Imhof et al., 1992), which occur frequently but on small timescales (<1 s). O'Brien et al. (2003) statistically analyzed the occurrence of these microbursts during geomagnetic events, showing that microbursts tend to occur most prominently in the pre-dawn and morning sectors (0–6 and 6–12 hr in MLT respectively), increasing rapidly before the epoch time (minimum Dst) and gradually reducing throughout the recovery phase. Around the epoch time, large occurrence rates reach L-shells down to around $L = 3–4$, in line with our results, suggesting that microbursts could be a significant contributor to the enhanced loss processes shown by our analysis.

Drivers of the enhanced loss processes are unlikely to be a result of a singular phenomenon. The increase in r up until t_{epoch} is observed in all four MLT quadrants, but following t_{epoch}, r remains elevated throughout much of the recovery phase on the dawnside, differently to the duskside in which r reduces again very early in the recovery phase. This suggests that the mechanism responsible for the initial loss is applicable in all MLT. A candidate for such is magnetopause shadowing. The initial compression of the magnetopause causes the loss of particles on the dayside, but within minutes, azimuthal particle drift can cause the entire outer region of the outer radiation belt to be lost. Empirical models (e.g., Shue et al., 1997, 1998) show that the dayside magnetopause can reach L-shells as close as $L = 8.5$ during geomagnetic activity, though recent studies of magnetopause crossings have shown that the magnetopause can be present much closer to Earth (e.g., Staples et al., 2020). In any case, $L = 8.5$ is far outside the range of this analysis, but the resulting outward radial diffusion due to the steep gradient in phase space density can cause the loss of electrons from the regions being analyzed here. The processes mentioned resulting from magnetopause shadowing only refer to the changes in the trapped flux. As stated previously, we expect that if there is a reduction in the trapped flux there should also be a proportionate reduction in the BLC flux and hence, no change in r. The observation that r increases during these times shows that the BLC flux decreases less than the trapped, signaling the presence of heightened atmospheric loss processes as well as magnetopause loss and transport of trapped electrons.

Figures 4g–4i show high r (10^{-1}, or 10% BLC to trapped ratio) inside $L = 3$, however, both trapped and BLC fluxes are low. Outside $L = 3.0$, r is highly variable in space and with activity level, with several features emerging with increasing AE. At $L > 5$ and around 21–5 MLT through midnight, r increases by around one order of magnitude from low to high activity (from around 10^{-2} to 10^{-1}), resulting from the decrease in trapped flux in the same region, but importantly, not in the BLC flux. Reductions in trapped flux in this region has been shown in other studies (e.g., Ni et al., 2016) to be a sign of magnetopause shadowing on the dayside and drift shell splitting at equatorial latitudes. However, at SAMPEX altitudes, even the largest pitch angles (i.e., 90°) map to very low equatorial pitch angles and are unlikely to be affected by magnetopause shadowing or drift shell splitting. This suggests that loss in this region is enhanced, driven by increased scattering of pitch angles. It is conceivable that whistler-mode chorus activity driven by substorm injections, which can subsequently cause the loss of electrons to the atmosphere (e.g., Jaynes et al., 2015), could account for this loss, as this would not necessarily affect >600 keV trapped flux. Injections cannot be directly inferred from this analysis, however, and should be studied further.

We also observe increasing r around 13–22 MLT and between $L = 3.0$–5.0 as a result of the increased BLC flux and lack of an increase in the trapped flux. This region is still faintly visible in the low activity, remaining around $r = 10^{-2}$, but increases by between half and a full order of magnitude during periods of high activity. At $L > 5.0$, r is at its maximum of 10^{-1}. The increased r in these regions is similar to Meredith et al. (2018). Figure 4 where plasmaspheric hiss is confined, also parameterized by AE in a similar way. We may be observing the effects of plasmaspheric hiss in our analysis. In the Meredith et al. (2018) study, they also observe high plasmaspheric hiss power below $L = 3.0$ on the dayside, the effects of which are not observed here due to the generally low BLC and trapped fluxes in this region.

Figure 4 also shows that r increases by around half an order of magnitude in the high activity where $L > 2.5$–3.0 in the pre-noon sector (6–12 MLT) and partially in the 0–6 sector, from around 4 MLT. This is also shown to a greater extent in the BLC flux, but the other prominent features may be hiding this in the r plot. This may be further evidence for whistler-mode chorus wave-induced precipitation as also observed in the SEA. Past studies have shown comparisons between observed BLC flux at low altitude and chorus but at lower energies using the POES mission >30 keV observations (e.g., Lam et al., 2010), while others (e.g., Meredith et al., 2011) have done so for several 100's of keV electrons. These studies show a link between increased dawnside precipitation and whistler-mode chorus activity. Meredith et al. (2013) presented a comprehensive whistler-mode chorus intensity database with detailed structure in L, MLT, latitude, and frequency. The lower-band chorus intensity >30° in latitude could be responsible for the apparent increases in the loss processes we observe here. The analysis of more active times in Meredith et al. (2020), Figures 2i and 2l both show high-intensity chorus across the dawn sectors, most intense during the pre-noon (6–12 hr MLT) sector. The lower bound of their highest intensities is around $L = 4$, though some less intense chorus can be seen as low at $L = 3$. The analysis in Meredith et al. (2020) is a further indication that chorus could be a main contributor to the features seen in our analysis.

Enhancements in loss and relative loss, shown in Figure 4 persist beyond the already discussed regions of whistler-mode chorus and plasmaspheric hiss, so other candidates for >0.63 MeV electron precipitation must be considered. Typically, EMIC waves are considered effective at scattering pitch angles into the loss cone for electrons of several hundreds keV (e.g., Hendry et al., 2017). These are typically associated with the post-noon sector (12–18 hr in MLT) but at L-shells around and above geosynchronous ($L \approx 6.6$; Usanova et al., 2012), which is outside of our analysis ranges. However, some studies (e.g., Halford et al., 2016; Jun et al., 2021; Meredith et al., 2014) have shown that EMIC waves can be observed at L-shells as low as $L = 3$–6 during storm conditions, which is in line with some regions of increased r in Figure 4i. Our analysis may therefore be showing signatures of EMIC waves during periods of high AE. While EMIC waves are most prominent during the main phase of storms, where we see the highest AE in Figures 2 and 3, Halford et al. (2010, 2016) show that they can persist throughout the recovery phase, which could be contributing to the sustained increased r in our SEA analyses.

Direct scattering via ULF waves could also be a possible contributor to the enhanced relative loss in our analysis. Loss cone modulation (Brito et al., 2015; Rae et al., 2018) is thought to be effective at scattering electrons into the BLC on the dayside and nightside magnetosphere following a compression of the magnetopause. Our analysis in Figure 4 shows increasing relative loss with activity at outer L-shells ($L > 4.5$) on the dayside most prominently, but also on the nightside. This could, however, also be a signature of whistler-mode chorus. ULF waves can also contribute to electron loss via modulation of plasmaspheric hiss (Breneman et al., 2015), which could also be a contributor here, as well as the possibility of combinations of other waves (Lee & Kim, 2020), though these effects in comparison to the effects already described are likely to be very small and not visible in this analysis.

6. Conclusions

We have statistically analyzed how >0.63 MeV electron flux in the BLC varies in relation to trapped flux, in order to find where the proportion of flux entering the BLC changes throughout a storm and during periods of high activity. We find:

1. Loss processes influencing >0.63 MeV electrons are enhanced outside the plasmapause during storm main phase
2. Enhanced loss processes are sustained throughout the recovery phase on the dawnside but diminish early in storm recovery phases across dusk

3. Analysis as a function of L-shell, MLT, and AE hints at a number of wave-modes that could be responsible for this, including whistler-mode chorus for dawnside losses and plasmaspheric hiss through dusk

These results provide further insight into the dynamics of the radiation belts during geomagnetic storms and other periods of high activity. We see an increase in the ratio of BLC flux to trapped flux where previous studies have shown enhancements in particular wave modes, suggesting a link between the two. These results enable us to partially separate observations of loss to the atmosphere from other loss mechanisms by comparing the change in the trapped flux to the change in the flux entering the precipitating flux. We have been able to show that although the BLC flux drops during storms, the processes of causing atmospheric loss is enhanced.

Data Availability Statement

Data from the SAMPEX PET instrument can freely be accessed at: http://www.srl.caltech.edu/sampex/Data-Center/data.html. Sym-H data used in the analysis and AE data used to generate the model plasmapause can be found via OMNIWeb: https://spdf.gsfc.nasa.gov/pub/data/omni/high_res_omni/.

References

Baker, D., Mason, G., Figueroa, O., Colon, G., Watzin, J., & Aleman, R. (1993). An overview of the Solar Anomalous, and Magnetospheric Particle Explorer (SAMPEX) mission. *IEEE Transactions on Geoscience and Remote Sensing*, *31*(3), 531–541. https://doi.org/10.1109/36.225519

Blum, L. W., Halford, A., Millan, R., Bonnell, J. W., Goldstein, J., Usanova, M., et al. (2015). Observations of coincident EMIC wave activity and duskside energetic electron precipitation on 18–19 January 2013. *Geophysical Research Letters*, *42*(14), 5727–5735. https://doi.org/10.1002/2015GL065245

Borovsky, J. E., & Denton, M. H. (2009). Electron loss rates from the outer radiation belt caused by the filling of the outer plasmasphere: The calm before the storm. *Journal of Geophysical Research: Space Physics*, *114*(A11), 11203. https://doi.org/10.1029/2009JA014063

Bortnik, J., & Thorne, R. (2007). The dual role of ELF/VLF chorus waves in the acceleration and precipitation of radiation belt electrons. *Journal of Atmospheric and Solar-Terrestrial Physics*, *69*(3), 378–386. https://doi.org/10.1016/J.JASTP.2006.05.030

Bortnik, J., Thorne, R. M., & Meredith, N. P. (2008). The unexpected origin of plasmaspheric hiss from discrete chorus emissions. *Nature*, *452*(7183), 62–66. https://doi.org/10.1038/nature06741

Bortnik, J., Thorne, R. M., O'Brien, T. P., Green, J. C., Strangeway, R. J., Shprits, Y. Y., & Baker, D. N. (2006). Observation of two distinct, rapid loss mechanisms during the 20 November 2003 radiation belt dropout event. *Journal of Geophysical Research*, *111*(A12), A12216. https://doi.org/10.1029/2006JA011802

Breneman, A. W., Halford, A., Millan, R., McCarthy, M., Fennell, J., Sample, J., et al. (2015). Global-scale coherence modulation of radiation-belt electron loss from plasmaspheric hiss. *Nature*, *523*(7559), 193–195. https://doi.org/10.1038/nature14515

Brito, T., Hudson, M. K., Kress, B., Paral, J., Halford, A., Millan, R., & Usanova, M. (2015). Simulation of ULF wave-modulated radiation belt electron precipitation during the 17 March 2013 storm. *Journal of Geophysical Research: Space Physics*, *120*(5), 3444–3461. https://doi.org/10.1002/2014JA020838

Carson, B. R., Rodger, C. J., & Clilverd, M. A. (2013). POES satellite observations of EMIC-wave driven relativistic electron precipitation during 1998–2010. *Journal of Geophysical Research: Space Physics*, *118*(1), 232–243. https://doi.org/10.1029/2012JA017998

Clilverd, M. A., Duthie, R., Hardman, R., Hendry, A. T., Rodger, C. J., Raita, T., et al. (2015). Electron precipitation from EMIC waves: A case study from 31 May 2013. *Journal of Geophysical Research: Space Physics*, *120*(5), 3618–3631. https://doi.org/10.1002/2015JA021090

Cook, W., Cummings, A., Cummings, J., Garrard, T., Kecman, B., Mewaldt, R., et al. (1993). PET: A proton/electron telescope for studies of magnetospheric, solar, and galactic particles. *IEEE Transactions on Geoscience and Remote Sensing*, *31*(3), 565–571. https://doi.org/10.1109/36.225523

Crew, A. B., Spence, H. E., Blake, J. B., Klumpar, D. M., Larsen, B. A., O'Brien, T. P., et al. (2016). First multipoint in situ observations of electron microbursts: Initial results from the NSF FIREBIRD II mission. *Journal of Geophysical Research: Space Physics*, *121*(6), 5272–5283. https://doi.org/10.1002/2016JA022485

Dietrich, S., Rodger, C. J., Clilverd, M. A., Bortnik, J., & Raita, T. (2010). Relativistic microburst storm characteristics: Combined satellite and ground-based observations. *Journal of Geophysical Research: Space Physics*, *115*(A12). https://doi.org/10.1029/2010JA015777

Douma, E., Rodger, C. J., Blum, L. W., & Clilverd, M. A. (2017). Occurrence characteristics of relativistic electron microbursts from SAMPEX observations. *Journal of Geophysical Research: Space Physics*, *122*(8), 8096–8107. https://doi.org/10.1002/2017JA024067

Engebretson, M. J., Posch, J. L., Wygant, J. R., Kletzing, C. A., Lessard, M. R., Huang, C. L., et al. (2015). Van Allen Probes, NOAA, GOES, and ground observations of an intense EMIC wave event extending over 12 hr in magnetic local time. *Journal of Geophysical Research A: Space Physics*, *120*(7), 5465–5488. https://doi.org/10.1002/2015JA021227

Forsyth, C., Rae, I. J., Murphy, K. R., Freeman, M. P., Huang, C.-L., Spence, H. E., et al. (2016). What effect do substorms have on the content of the radiation belts? *Journal of Geophysical Research: Space Physics*, *121*(7), 6292–6306. https://doi.org/10.1002/2016JA022620

Friedel, R., Reeves, G., & Obara, T. (2002). Relativistic electron dynamics in the inner magnetosphere—A review. *Journal of Atmospheric and Solar-Terrestrial Physics*, *64*(2), 265–282. https://doi.org/10.1016/S1364-6826(01)00088-8

Glauert, S. A., Horne, R. B., & Meredith, N. P. (2014). Simulating the Earth's radiation belts: Internal acceleration and continuous losses to the magnetopause. *Journal of Geophysical Research: Space Physics*, *119*(9), 7444–7463. https://doi.org/10.1002/2014JA020092

Goldstein, J., Sandel, B. R., Thomsen, M. F., Spasojević, M., & Reiff, P. H. (2004). Simultaneous remote sensing and in situ observations of plasmaspheric drainage plumes. *Journal of Geophysical Research: Space Physics*, *109*(A3). https://doi.org/10.1029/2003JA010281

Halford, A. J., Fraser, B. J., & Morley, S. K. (2010). EMIC wave activity during geomagnetic storm and nonstorm periods: CRRES results. *Journal of Geophysical Research: Space Physics*, *115*(12). https://doi.org/10.1029/2010JA015716

Halford, A. J., Fraser, B. J., & Morley, S. K. (2015). EMIC waves and plasmaspheric and plume density: CRRES results. *Journal of Geophysical Research A: Space Physics*, *120*(3), 1974–1992. https://doi.org/10.1002/2014JA020338

Halford, A. J., Fraser, B. J., Morley, S. K., Elkington, S. R., & Chan, A. A. (2016). Dependence of EMIC wave parameters during quiet, geomagnetic storm, and geomagnetic storm phase times. *Journal of Geophysical Research: Space Physics*, *121*(7), 6277–6291. https://doi.org/10.1002/2016JA022694

Hardman, R., Clilverd, M. A., Rodger, C. J., Brundell, J. B., Duthie, R., Holzworth, R. H., et al. (2015). A case study of electron precipitation fluxes due to plasmaspheric hiss. *Journal of Geophysical Research: Space Physics*, *120*(8), 6736–6748. https://doi.org/10.1002/2015JA021429

Hendry, A. T., Rodger, C. J., & Clilverd, M. A. (2017). Evidence of sub-MeV EMIC-driven electron precipitation. *Geophysical Research Letters*, *44*(3), 1210–1218. https://doi.org/10.1002/2016GL071807

Hendry, A. T., Rodger, C. J., Clilverd, M. A., & Morley, S. K. (2021). Evidence of sub-MeV EMIC-driven trapped electron flux dropouts from GPS observations. *Geophysical Research Letters*, *48*(9), e2021GL092664. https://doi.org/10.1029/2021GL092664

Hendry, A. T., Santolik, O., Kletzing, C. A., Rodger, C. J., Shiokawa, K., & Baishev, D. (2019). Multi-instrument observation of nonlinear EMIC-driven electron precipitation at sub-MeV energies. *Geophysical Research Letters*, *46*(13), 7248–7257. https://doi.org/10.1029/2019GL082401

Horne, R. B., & Thorne, R. M. (1998). Potential waves for relativistic electron scattering and stochastic acceleration during magnetic storms. *Geophysical Research Letters*, *25*(15), 3011–3014. https://doi.org/10.1029/98GL01002

Hutchinson, J. A., Wright, D. M., & Milan, S. E. (2011). Geomagnetic storms over the last solar cycle: A superposed epoch analysis. *Journal of Geophysical Research: Space Physics*, *116*(A9). https://doi.org/10.1029/2011JA016463

Imhof, W. L., Voss, H. D., Mobilia, J., Datlowe, D. W., Gaines, E. E., McGlennon, J. P., & Inan, U. S. (1992). Relativistic electron microbursts. *Journal of Geophysical Research*, *97*(A9), 13829–13837. https://doi.org/10.1029/92JA01138

Jaynes, A. N., Baker, D. N., Singer, H. J., Rodriguez, J. V., Loto'aniu, T. M., Ali, A. F., et al. (2015). Source and seed populations for relativistic electrons: Their roles in radiation belt changes. *Journal of Geophysical Research: Space Physics*, *120*(9), 7240–7254. https://doi.org/10.1002/2015JA021234

Jun, C. W., Miyoshi, Y., Kurita, S., Yue, C., Bortnik, J., Lyons, L., et al. (2021). The characteristics of EMIC waves in the magnetosphere based on the Van Allen Probes and Arase observations. *Journal of Geophysical Research: Space Physics*, *126*(6), e2020JA029001. https://doi.org/10.1029/2020JA029001

Kennel, C. F., & Petschek, H. E. (1966). Limit on stably trapped particle fluxes. *Journal of Geophysical Research*, *71*(1), 1–28. https://doi.org/10.1029/JZ071i001p00001

Klecker, B., Hovestadt, D., Scholer, M., Arbinger, H., Ertl, M., Kastele, H., et al. (1993). HILT: A heavy ion large area proportional counter telescope for solar and anomalous cosmic rays. *IEEE Transactions on Geoscience and Remote Sensing*, *31*(3), 542–548. https://doi.org/10.1109/36.225520

Kozyra, J. U., Cravens, T. E., Nagy, A. F., & Fontheim, E. G. (1984). Effects of energetic heavy ions on electromagnetic ion cyclotron wave generation in the plasmapause region. *Journal of Geophysical Research*, *89*(A4), 2217–2233. https://doi.org/10.1029/JA089iA04p02217

Lam, M. M., Horne, R. B., Meredith, N. P., & Glauert, S. A. (2007). Modeling the effects of radial diffusion and plasmaspheric hiss on outer radiation belt electrons. *Geophysical Research Letters*, *34*(20), 20112. https://doi.org/10.1029/2007GL031598

Lam, M. M., Horne, R. B., Meredith, N. P., Glauert, S. A., Moffat-Griffin, T., & Green, J. C. (2010). Origin of energetic electron precipitation >30 keV into the atmosphere. *Journal of Geophysical Research A: Space Physics*, *115*(A4), A00F08. https://doi.org/10.1029/2009JA014619

Lee, D. Y., & Kim, J. (2020). Simultaneous influence of whistler-mode chorus and EMIC waves on electron loss in the Earth's radiation belt. *Journal of the Korean Physical Society*, *77*(8), 707–713. https://doi.org/10.3938/jkps.77.707

Lejosne, S., & Kollmann, P. (2020). Radiation belt radial diffusion at Earth and beyond. *Space Science Reviews*, *216*(1). https://doi.org/10.1007/s11214-020-0642-6

Loto'aniu, T. M., Mann, I. R., Ozeke, L. G., Chan, A. A., Dent, Z. C., & Milling, D. K. (2006). Radial diffusion of relativistic electrons into the radiation belt slot region during the 2003 Halloween geomagnetic storms. *Journal of Geophysical Research*, *111*, 4218. https://doi.org/10.1029/2005JA011355

Lyons, L. R., & Thorne, R. M. (1972). Parasitic pitch angle diffusion of radiation belt particles by ion cyclotron waves. *Journal of Geophysical Research*, *77*(28), 5608–5616. https://doi.org/10.1029/JA077i028p05608

Mann, I. R., Ozeke, L. G., Murphy, K. R., Claudepierre, S. G., Turner, D. L., Baker, D. N., et al. (2016). Explaining the dynamics of the ultra-relativistic third Van Allen radiation belt. *Nature Physics*, *12*(10), 978–983. https://doi.org/10.1038/nphys3799

Meredith, N. P., Cain, M., Horne, R. B., Thorne, R. M., Summers, D., & Anderson, R. R. (2003). Evidence for chorus-driven electron acceleration to relativistic energies from a survey of geomagnetically disturbed periods. *Journal of Geophysical Research*, *108*(A6), 1248. https://doi.org/10.1029/2002JA009764

Meredith, N. P., Horne, R. B., Bortnik, J., Thorne, R. M., Chen, L., Li, W., & Sicard-Piet, A. (2013). Global statistical evidence for chorus as the embryonic source of plasmaspheric hiss. *Geophysical Research Letters*, *40*(12), 2891–2896. https://doi.org/10.1002/GRL.50593

Meredith, N. P., Horne, R. B., Clilverd, M. A., Horsfall, D., Thorne, R. M., & Anderson, R. R. (2006). Origins of plasmaspheric hiss. *Journal of Geophysical Research: Space Physics*, *111*(9), A09217. https://doi.org/10.1029/2006JA011707

Meredith, N. P., Horne, R. B., Glauert, S. A., & Anderson, R. R. (2007). Slot region electron loss timescales due to plasmaspheric hiss and lightning-generated whistlers. *Journal of Geophysical Research: Space Physics*, *112*(8). https://doi.org/10.1029/2007JA012413

Meredith, N. P., Horne, R. B., Glauert, S. A., Thorne, R. M., Summers, D., Albert, J. M., & Anderson, R. R. (2006). Energetic outer zone electron loss timescales during low geomagnetic activity. *Journal of Geophysical Research: Space Physics*, *111*(5). https://doi.org/10.1029/2005JA011516

Meredith, N. P., Horne, R. B., Iles, R. H., Thorne, R. M., Heynderickx, D., & Anderson, R. R. (2002). Outer zone relativistic electron acceleration associated with substorm-enhanced whistler-mode chorus. *Journal of Geophysical Research: Space Physics*, *107*(A7), SMP29-1–SMP29-14. https://doi.org/10.1029/2001JA900146

Meredith, N. P., Horne, R. B., Kersten, T., Fraser, B. J., & Grew, R. S. (2014). Global morphology and spectral properties of EMIC waves derived from CRRES observations. *Journal of Geophysical Research: Space Physics*, *119*(7), 5328–5342. https://doi.org/10.1002/2014JA020064

Meredith, N. P., Horne, R. B., Kersten, T., Li, W., Bortnik, J., Sicard, A., & Yearby, K. H. (2018). Global model of plasmaspheric hiss from multiple satellite observations. *Journal of Geophysical Research: Space Physics*, *123*(6), 4526–4541. https://doi.org/10.1029/2018JA025226

Meredith, N. P., Horne, R. B., Lam, M. M., Denton, M. H., Borovsky, J. E., & Green, J. C. (2011). Energetic electron precipitation during high-speed solar wind stream driven storms. *Journal of Geophysical Research: Space Physics*, *116*(5). https://doi.org/10.1029/2010JA016293

Meredith, N. P., Horne, R. B., Shen, X., Li, W., & Bortnik, J. (2020). Global model of whistler-mode chorus in the near-equatorial region ($|\lambda_m| < 18°$). *Geophysical Research Letters*, *47*(11), e2020GL087311. https://doi.org/10.1029/2020GL087311

Millan, R., & Thorne, R. (2007). Review of radiation belt relativistic electron losses. *Journal of Atmospheric and Solar-Terrestrial Physics*, *69*(3), 362–377. https://doi.org/10.1016/J.JASTP.2006.06.019

Miyoshi, Y., & Kataoka, R. (2008). Flux enhancement of the outer radiation belt electrons after the arrival of stream interaction regions. *Journal of Geophysical Research: Space Physics*, *113*(A3). https://doi.org/10.1029/2007JA012506

Murphy, K. R., Watt, C. E. J., Mann, I. R., Jonathan Rae, I., Sibeck, D. G., Boyd, A. J., et al. (2018). The global statistical response of the outer radiation belt during geomagnetic storms. *Geophysical Research Letters*, *45*(9), 3783–3792. https://doi.org/10.1002/2017GL076674

Ni, B., Zou, Z., Li, X., Bortnik, J., Xie, L., & Gu, X. (2016). Occurrence characteristics of outer zone relativistic electron butterfly distribution: A survey of Van Allen Probes REPT measurements. *Geophysical Research Letters*, *43*(11), 5644–5652. https://doi.org/10.1002/2016GL069350

O'Brien, T. P., Lorentzen, K. R., Mann, I. R., Meredith, N. P., Blake, J. B., Fennell, J. F., et al. (2003). Energization of relativistic electrons in the presence of ULF power and MeV microbursts: Evidence for dual ULF and VLF acceleration. *Journal of Geophysical Research: Space Physics*, *108*(A8), 1329. https://doi.org/10.1029/2002JA009784

O'Brien, T. P., & Moldwin, M. B. (2003). Empirical plasmapause models from magnetic indices. *Geophysical Research Letters*, *30*(4). https://doi.org/10.1029/2002GL016007

Olifer, L., Mann, I. R., Ozeke, L. G., Rae, I. J., & Morley, S. K. (2019). On the relative strength of electric and magnetic ULF wave radial diffusion during the March 2015 geomagnetic storm. *Journal of Geophysical Research: Space Physics*, *124*(4), 2018JA026348. https://doi.org/10.1029/2018JA026348

Qin, M., Hudson, M., Millan, R., Woodger, L., & Shekhar, S. (2018). Statistical investigation of the efficiency of EMIC waves in precipitating relativistic electrons. *Journal of Geophysical Research: Space Physics*, *123*(8), 6223–6230. https://doi.org/10.1029/2018JA025419

Rae, I. J., Murphy, K. R., Watt, C. E., Halford, A. J., Mann, I. R., Ozeke, L. G., et al. (2018). The role of localized compressional ultra-low frequency waves in energetic electron precipitation. *Journal of Geophysical Research: Space Physics*, *123*(3), 1900–1914. https://doi.org/10.1002/2017JA024674

Reeves, G. D., McAdams, K. L., Friedel, R. H. W., & O'Brien, T. P. (2003). Acceleration and loss of relativistic electrons during geomagnetic storms. *Geophysical Research Letters*, *30*(10). https://doi.org/10.1029/2002GL016513

Reidy, J. A., Horne, R. B., Glauert, S. A., Clilverd, M. A., Meredith, N. P., Woodfield, E. E., et al. (2021). Comparing electron precipitation fluxes calculated from pitch angle diffusion coefficients to LEO satellite observations. *Journal of Geophysical Research: Space Physics*, *126*(3), e2020JA028410. https://doi.org/10.1029/2020JA028410

Rodger, C. J., Carson, B. R., Cummer, S. A., Gamble, R. J., Clilverd, M. A., Green, J. C., et al. (2010). Contrasting the efficiency of radiation belt losses caused by ducted and nonducted whistler-mode waves from ground-based transmitters. *Journal of Geophysical Research: Space Physics*, *115*(12). https://doi.org/10.1029/2010JA015880

Rodger, C. J., Clilverd, M. A., Green, J. C., & Lam, M. M. (2010). Use of POES SEM-2 observations to examine radiation belt dynamics and energetic electron precipitation into the atmosphere. *Journal of Geophysical Research: Space Physics*, *115*(A4) . https://doi.org/10.1029/2008JA014023

Rodger, C. J., Hendry, A. T., Clilverd, M. A., Kletzing, C. A., Brundell, J. B., & Reeves, G. D. (2015). High-resolution in situ observations of electron precipitation-causing EMIC waves. *Geophysical Research Letters*, *42*(22), 9633–9641. https://doi.org/10.1002/2015GL066581

Rodger, C. J., Kavanagh, A. J., Clilverd, M. A., & Marple, S. R. (2013). Comparison between POES energetic electron precipitation observations and riometer absorptions: Implications for determining true precipitation fluxes. *Journal of Geophysical Research: Space Physics*, *118*(12), 7810–7821. https://doi.org/10.1002/2013JA019439

Ross, J. P. J., Glauert, S. A., Horne, R. B., Watt, C. E., Meredith, N. P., & Woodfield, E. E. (2020). A new approach to constructing models of electron diffusion by EMIC waves in the radiation belts. *Geophysical Research Letters*, *47*(20), e2020GL088976. https://doi.org/10.1029/2020GL088976

Selesnick, R. S. (2015). Measurement of inner radiation belt electrons with kinetic energy above 1 MeV. *Journal of Geophysical Research A: Space Physics*, *120*(10), 8339–8349. https://doi.org/10.1002/2015JA021387

Shue, J.-H., Chao, J. K., Fu, H. C., Russell, C. T., Song, P., Khurana, K. K., & Singer, H. J. (1997). A new functional form to study the solar wind control of the magnetopause size and shape. *Journal of Geophysical Research: Space Physics*, *102*(A5), 9497–9511. https://doi.org/10.1029/97JA00196

Shue, J.-H., Song, P., Russell, C. T., Steinberg, J. T., Chao, J. K., Zastenker, G., et al. (1998). Magnetopause location under extreme solar wind conditions. *Journal of Geophysical Research: Space Physics*, *103*(A8), 17691–17700. https://doi.org/10.1029/98JA01103

Sigsbee, K., Kletzing, C. A., Faden, J. B., Jaynes, A. N., Reeves, G. D., & Jahn, J. (2020). Simultaneous observations of electromagnetic ion cyclotron (EMIC) waves and pitch angle scattering during a Van Allen Probes conjunction. *Journal of Geophysical Research: Space Physics*, *125*(4), e2019JA027424. https://doi.org/10.1029/2019JA027424

Smith, E. J., Frandsen, A. M. A., Tsurutani, B. T., Thorne, R. M., & Chan, K. W. (1974). Plasmaspheric hiss intensity variations during magnetic storms. *Journal of Geophysical Research*, *79*(16), 2507–2510. https://doi.org/10.1029/ja079i016p02507

Staples, F. A., Rae, I. J., Forsyth, C., Smith, A. R. A., Murphy, K. R., Raymer, K. M., et al. (2020). Do statistical models capture the dynamics of the magnetopause during sudden magnetospheric compressions? *Journal of Geophysical Research: Space Physics*, *125*(4), e2019JA027289. https://doi.org/10.1029/2019JA027289

Summers, D., Ni, B., & Meredith, N. P. (2007). Timescales for radiation belt electron acceleration and loss due to resonant wave-particle interactions: 2. Evaluation for VLF chorus, ELF hiss, and electromagnetic ion cyclotron waves. *Journal of Geophysical Research: Space Physics*, *112*(A4). https://doi.org/10.1029/2006JA011993

Thorne, R. M. (2010). Radiation belt dynamics: The importance of wave-particle interactions. *Geophysical Research Letters*, *37*(22). https://doi.org/10.1029/2010GL044990

Thorne, R. M., Li, W., Ni, B., Ma, Q., Bortnik, J., Chen, L., et al. (2013). Rapid local acceleration of relativistic radiation-belt electrons by magnetospheric chorus. *Nature*, *504*(7480), 411–414. https://doi.org/10.1038/nature12889

Thorne, R. M., Smith, E. J., Burton, R. K., & Holzer, R. E. (1973). Plasmaspheric hiss. *Journal of Geophysical Research*, *78*(10), 1581–1596. https://doi.org/10.1029/JA078I010P01581

Tsurutani, B. T., Smith, E. J., & Thorne, R. M. (1975). Electromagnetic hiss and relativistic electron losses in the inner zone. *Journal of Geophysical Research*, *80*(4), 600–607. https://doi.org/10.1029/ja080i004p00600

Usanova, M. E., Darrouzet, F., Mann, I. R., & Bortnik, J. (2013). Statistical analysis of EMIC waves in plasmaspheric plumes from Cluster observations. *Journal of Geophysical Research: Space Physics*, *118*(8), 4946–4951. https://doi.org/10.1002/jgra.50464

Usanova, M. E., Drozdov, A., Orlova, K., Mann, I. R., Shprits, Y., Robertson, M. T., et al. (2014). Effect of EMIC waves on relativistic and ultra-relativistic electron populations: Ground-based and Van Allen Probes observations. *Geophysical Research Letters*, *41*(5), 1375–1381. https://doi.org/10.1002/2013GL059024

Usanova, M. E., Mann, I. R., Bortnik, J., Shao, L., & Angelopoulos, V. (2012). THEMIS observations of electromagnetic ion cyclotron wave occurrence: Dependence on AE, SYMH, and solar wind dynamic pressure. *Journal of Geophysical Research: Space Physics*, *117*(A10). https://doi.org/10.1029/2012JA018049

Walach, M., & Grocott, A. (2019). SuperDARN observations during geomagnetic storms, geomagnetically active times, and enhanced solar wind driving. *Journal of Geophysical Research: Space Physics*, *124*(7), 5828–5847. https://doi.org/10.1029/2019JA026816

Walton, S. D., Forsyth, C., Rae, I. J., Watt, C. E. J., Thompson, R. L., Horne, R. B., et al. (2021). Cross-L* coherence of the outer radiation belt during storms and the role of the plasmapause. *Journal of Geophysical Research: Space Physics*, e2021JA029308. https://doi.org/10.1029/2021JA029308

Wang, H., He, Y., Lühr, H., Kistler, L., Saikin, A., Lund, E., & Ma, S. (2019). Storm time EMIC waves observed by swarm and Van Allen Probe satellites. *Journal of Geophysical Research: Space Physics*, *124*(1), 293–312. https://doi.org/10.1029/2018JA026299

Yokoyama, N. (1997). Statistical nature of geomagnetic storms. *Journal of Geophysical Research A: Space Physics*, *102*(A7), 14215–14222. https://doi.org/10.1029/97JA00903

Zhang, X.-J., Li, W., Thorne, R. M., Angelopoulos, V., Bortnik, J., Kletzing, C. A., et al. (2016). Statistical distribution of EMIC wave spectra: Observations from Van Allen Probes. *Geophysical Research Letters*, *43*(24), 12348–12355. https://doi.org/10.1002/2016GL071158